3D finite-difference dynamic-rupture modeling along nonplanar faults

Víctor M. Cruz-Atienza[1], Jean Virieux[2], and Hideo Aochi[3]

ABSTRACT

Proper understanding of seismic emissions associated with the growth of complexly shaped microearthquake networks and larger-scale nonplanar fault ruptures, both in arbitrarily heterogeneous media, requires accurate modeling of the underlying dynamic processes. We present a new 3D dynamic-rupture, finite-difference model called the finite-difference, fault-element (FDFE) method; it simulates the dynamic rupture of nonplanar faults subjected to regional loads in complex media. FDFE is based on a 3D methodology for applying dynamic-rupture boundary conditions along the fault surface. The fault is discretized by a set of parallelepiped fault elements in which specific boundary conditions are applied. These conditions are applied to the stress tensor, once transformed into a local fault reference frame. Numerically determined weight functions multiplying particle velocities around each element allow accurate estimates of fault kinematic parameters (i.e., slip and slip rate) independent of faulting mechanism. Assuming a Coulomb-like slip-weakening friction law, a parametric study suggests that the FDFE method converges toward a unique solution, provided that the cohesive zone behind the rupture front is well resolved (i.e., four or more elements inside this zone). Solutions are free of relevant numerical artifacts for grid sizes smaller than approximately 70 m. Results yielded by the FDFE approach are in good quantitative agreement with those obtained by a semianalytical boundary integral method along planar and nonplanar parabola-shaped faults. The FDFE method thus provides quantitative, accurate results for spontaneous-rupture simulations on intricate fault geometries.

INTRODUCTION

The permeability of oil reservoirs represents one of the most prominent characterization parameters for hydrocarbon production. This parameter evolves with time during oil extraction as a result of microearthquake activity and rock compaction induced by hydraulic stress changes (Royer and Voillemont, 2005). The variation of permeability may induce fluid migration and extraction mitigation. A seismicity-based methodology allowing global reservoir characterization may help track fluid migration and adapt exploitation strategies (Shapiro et al., 2002; Shapiro et al., 2005). The dynamic growth of complexly shaped fracture networks is thus a fundamental issue that should be understood. In the last few years, efforts have been made to develop new 3D numerical methods when considering nonplanar rupture propagation. Important implications in the fracture energy balance have been identified when the rupture front abruptly changes its direction of propagation (Adda-Bedia and Madariaga,

2005; Madariaga and Ampuero, 2005; Vilotte et al., 2005). Consequently, the absence of realistic fault geometries when modeling real data may result in misleading conclusions, especially when interpreting seismic emissions.

Fault interaction and branching may be enhanced by specific regional loads (Aochi et al., 2002; Oglesby et al., 2003; Ando et al., 2004; Aochi et al., 2005). In these cases, rupture propagation is governed mainly by the friction parameters, the rupture velocity, and the orientation of fault branches, which entirely determine the two competing forces: the fault strength and the shear stresses ahead of the rupture front (Kame et al., 2003; Cruz-Atienza et al., 2004; Aochi et al., 2005). The dynamic fault-normal stress changes translated into strength fluctuations are often negligible in realistic nonplanar rupture conditions if they occur far from the free surface (Aochi et al., 2000a; Aochi and Fukuyama, 2002). Almost all of these results have been obtained with boundary integral methods (BIE), which are highly adapted and accurate approaches for solving geometrically

[1]Formerly Géosciences Azur, UNSA-CNRS, Sophia-Antipolis, France; presently San Diego State University, Department of Geological Sciences, San Diego, California. E-mail: cruz@sciences.sdsu.edu.
[2]Géosciences Azur, UNSA-CNRS, Sophia-Antipolis, France. E-mail: virieux@geoazur.unice.fr.
[3]Bureau de Recherches Géologiques et Minières, Orléans, France. E-mail: h.aochi@brgm.fr.

complex problems. However, most of them may become rapidly expensive because the spatiotemporal convolution involved in the integral equations often requires a total calculation time proportional to the square of the number of grid elements multiplied by the number of time steps. Moreover, they use analytical Green functions, which directly depend on properties of the propagation medium; so only homogeneous full spaces can be considered. In other words, feedback interactions between the source and its environment are strongly constrained to simple, often unrealistic conditions.

On the other hand, standard and spectral finite-element methods (e.g., Oglesby, 1999; Aagaard, 2000; Ampuero and Vilotte, 2002; Vilotte et al., 2005; Ely et al., 2006), which handle arbitrarily heterogeneous media as finite-difference methods do, are generally computationally intensive. This limitation has prevented scientists from exploring systematically different mechanical models in large-scale earthquake simulations to perform statistical analysis of results. A promising, fast, and accurate 2D dynamic-rupture, finite-volume technique is proposed by Benjemaa et al. (2007). This technique handles unstructured mesh refinement around nonplanar free surfaces and faults embedded in arbitrarily heterogeneous materials. Nevertheless, until the 3D extension exists, it cannot be used to analyze seismic data.

For many years, finite-difference methods have been used for modeling earthquake rupture dynamics on planar faults (Andrews, 1976b; Madariaga, 1976; Mikumo and Miyatake, 1978; Day, 1982; Virieux and Madariaga, 1982; Olsen et al., 1997; Madariaga et al., 1998). Nonuniform grid spacing has allowed Mikumo and Miyatake (1993) to study rupture processes of real earthquakes on planar dipping faults. A similar technique is proposed by Zhang et al. (2006) using the standard staggered grid (Madariaga, 1976; Virieux, 1986). A few years ago, Cruz-Atienza et al. (2002) introduced a finite-difference approach capable of modeling the dynamic rupture of arbitrary nonplanar faults (for details, see Cruz-Atienza and Virieux, 2004). Preliminary results in three dimensions with this model were first obtained for the 1992 Landers (Mw = 7.3) earthquake, considering its real geometry (Cruz-Atienza et al., 2004).

However, recent validation efforts conducted for the dynamic-rupture problem have revealed that several well-established numerical models have important accuracy problems (Harris and Archuleta, 2004), especially those finite-difference approaches describing the source with a thick-fault numerical discretization (Dalguer and Day, 2006). Most of the methods mentioned above belong to this family of approaches. Particular attention should then be paid when using them and, even more, when introducing new methodologies inspired by the thick-fault strategy. Validation of these methods should necessarily include comparisons with completely independent methods, such as semianalytical boundary integrals or spectral-element approaches.

In this paper, we introduce, analyze, and validate, in three dimensions, the finite-difference methodology proposed by Cruz-Atienza and Virieux (2004) in two dimensions. Thus, our approach allows the dynamic-rupture simulation of 3D nonplanar faults embedded in arbitrarily heterogeneous media and governed by slip-dependent friction laws.

We first state the elastodynamic equations for the dynamic-rupture problem and the way rupture boundary conditions are applied in our 3D finite-difference technique. After a convergence analysis in terms of the cohesive-zone resolution, we validate the methodology by comparing results for spontaneous slip-weakening ruptures along planar and nonplanar (curvilinear) faults against those obtained with

an independent BIE approach (Aochi et al., 2000b). This comparison shows that our finite-difference rupture model, based on a thick-fault source description, is accurate enough to perform these complex simulations. Moreover, it confirms that finite-difference (FD) techniques still represent a viable and reliable way to model earthquake dynamics along nonplanar complexly shaped fault networks in three dimensions.

NUMERICAL MODEL

The numerical approach introduced in this section is basically an extension to three dimensions of the finite-difference fault-element (FDFE) model proposed by Cruz-Atienza and Virieux (2004) in two dimensions. In that work, Cruz-Atienza and Virieux show that finite-difference approaches in a regular grid are able to model the dynamic rupture of faults having nonplanar (curvilinear) geometries. A key element of that approach is the way rupture-boundary conditions are implemented. The two-dimensional analysis shows that the scaling between grid size and number of grid nodes within a source controls the accuracy of the method and makes it possible to discretize the same source in many equivalent ways by reducing the spatial grid step and increasing the number of stress grid points involved in boundary conditions.

When modeling huge 3D rupture scenarios, computational resources prevent the use of extremely fine meshes; however, fracture discretizations with moderate numbers of stress grid points are suitable for obtaining accurate enough results. As we shall see, other parameters also play an important role, especially in the numerical convergence of the method. Before introducing the dynamic-rupture model, let us first state the equations for this problem and the way they are approximated numerically.

Consider a linearly elastic 3D homogeneous and isotropic medium, fully described by the Lamé coefficients λ and μ and the density ρ. Following Madariaga (1976), in the absence of body forces, the elastodynamic equations governing the P- and S-wave propagation in such a medium may be expressed in terms of the velocity vector $\mathbf{v}_i$ and the stress tensor $\boldsymbol{\tau}_{ij}$ as

$$\rho \frac{\partial \mathbf{v}_i}{\partial t} = \boldsymbol{\tau}_{ij,j}, \tag{1a}$$

$$\frac{\partial \boldsymbol{\tau}_{ij}}{\partial t} = \lambda \mathbf{v}_{k,k} \delta_{ij} + \mu (\mathbf{v}_{i,j} + \mathbf{v}_{j,i}). \tag{1b}$$

System 1 contains nine partial differential equations that may be discretized in a partly staggered finite-difference grid where velocities and stresses are known in two separated, regular lattices (Saenger et al., 2000) as shown in Figure 1. The spatial differential operators of system 1 are deduced by Cruz-Atienza (2006) following Saenger et al. (2000). Numerical finite-difference stencils for first derivatives along the three Cartesian directions are given in Appendix A. Note that the current leapfrog partly staggered approach retains the efficiency of the standard finite-difference staggered grid: One must estimate stress derivatives at velocity grid points, and conversely, velocity derivatives at stress locations. Figure 1 shows the stencil of the second-order spatial operators applied to the velocity field (black spheres) to compute a stress-point value (gray cube). In the present work, we apply both second- and fourth-order accurate operators in the space increment (Cruz-Atienza and Virieux, 2004). For the sake of computational efficiency, time derivatives are always performed with a second-order-accurate leapfrog integration.

Two main advantages of the partly staggered finite-difference approach with respect to the standard staggered grid (Madariaga, 1976; Virieux, 1986) should be pointed out: (1) the stress and the velocity fields are defined in different nodes, each field having all of its components at the same node, and (2) the stability condition is less restrictive. As we shall see, the first advantage leads us to one fundamental aspect of the proposed finite-difference approach because it allows the stress-tensor transformation needed for the application of rupture boundary conditions of an arbitrary nonplanar-oriented crack. Concerning the second one, the von Neumann stability analysis shows that the magic time step given by $\Delta t \leq h/V_{max}$, where h and Δt are, respectively, the spatial and time steps and V_{max} is the maximum P-wave speed in the model, satisfies the stability condition if second-order spatial operators are applied (Saenger et al., 2000). In contrast with the standard staggered grid, the stability condition does not depend on the problem dimension. Moreover, if using fourth-order spatial operators in their stability limit, the time step on the partly staggered grid is 1.7 times higher than that of the standard grid. This translates into 40% fewer iterations to achieve the same simulation problem. Of course, these are theoretical values computed for planar waves propagating in homogeneous unbounded spaces.

Imposing dynamic rupture-boundary conditions always makes the stability criteria more restrictive. Values for the Courant number $V_{max}\Delta t/h$ up to 0.66 yield stable solutions when simulating the spontaneous rupture in the partly staggered grid with our numerical approach. This limit is at least 1.5 times greater than those reported in previous finite-difference rupture models (e.g., Virieux and Madariaga, 1982; Madariaga et al., 1998). Even if higher-order schemes are expected to verify more restrictive stability conditions than those of low order, this Courant value is valid for the fourth-order spatial operators we use throughout this study.

To simulate an unbounded space without loss of accuracy, we have implemented the perfectly matched layer (PML) absorbing boundary conditions in every external boundary of the 3D computational domain (Berenger, 1994; Collino and Tsogka, 2001; Marcinkovich and Olsen, 2003). Numerical tests in heterogeneous media show an effective energy absorption greater than 99% (Cruz-Atienza, 2006). Before analyzing the numerical properties of the rupture model, let us first introduce the way a source is discretized and how rupture-boundary conditions are applied along an arbitrarily shaped 3D surface.

Source discretization

Following the 2D strategy introduced by Cruz-Atienza and Virieux (2004), a given finite-rupture surface is represented numerically by a set of neighboring fault elements placed alongside this surface. (In the 2D model, the fault elements are called numerical cells.) A source fault element is a well-structured set of stress grid points that acts as an elementary source unity. This means that local boundary conditions are applied on each element, depending on the orientation of the local fault-normal vector.

A fault element describes a 45° rotated parallelepiped such as the one shown in Figure 2 (gray cubes). We found this specific element structure, with 65 stress grid points, achieved the best results for grid sizes ranging from 20 to 70 m (Cruz-Atienza, 2006). As we conclude in the Resolution and Convergence section, high-order elements (i.e., elements with a large number of stress grid points) in relatively coarse meshes affect rupture solutions because of the long distances separating their central points. The number of stress grid points along the diagonals parallel to the x- and y-axes is the same as the stress grid layers perpendicular to the z-axis. In this case, the element rotation is with respect to the z-axis. However, for symmetry reasons, it may be with respect to any of the three Cartesian axes.

Note also that this element configuration results in only two of its faces (i.e., the upper and bottom faces in Figure 2b) being parallel to one of the Cartesian planes. Consequently, the way to discretize nonplanar fault surfaces is by forcing the source geometry to have a translation-invariant direction parallel to the rotation axis of the fault elements. In our example, such a translation-invariant direction is
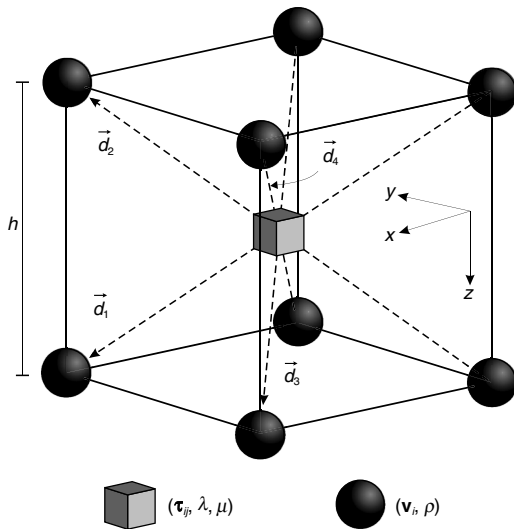

Figure 1. Three-dimensional second-order, finite-difference stencil used for computing spatial derivatives of the velocity field $\mathbf{v}_i$ in a stress tensor $\boldsymbol{\tau}_{ij}$ location along the three Cartesian directions. An analogous stencil is used for computing stress derivatives in velocity locations. Second-order finite differences involved in this stencil (Appendix A) are calculated along the four Cartesian axis bisectors ($\mathbf{d}_i$). The quantity h is the spatial grid step, whereas the medium properties are given by the Lamé coefficients λ and μ and the density ρ. All velocity and stress components are known at one single node.
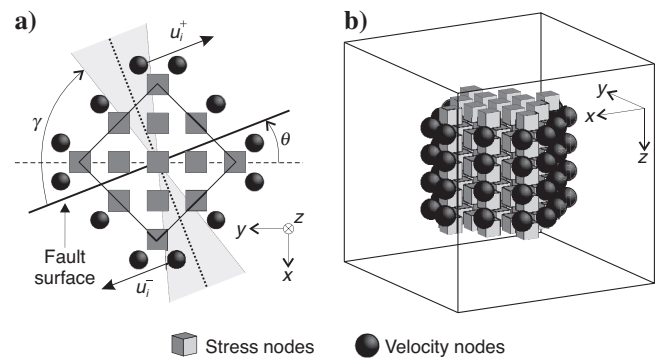

Figure 2. (a) Upper view of one fault element. In this example, the translation-invariant axis is parallel to the z Cartesian axis. The angle θ gives the fault-plane orientation with respect to that axis (see also Figure 3). The angle γ determines the spacial sector (gray region) around the fault-normal direction (dotted line) used to compute the slip and slip-rate functions (see section on Rupture Kinematics). (b) Three-dimensional perspective view of one individual fault element.

the z-axis. The discretization of a finite source may then be performed in two stages. First, the nonplanar source geometry is mapped over the x-y Cartesian plane by a succession of fault elements placed beside each other in a way similar to the 2D model. Second, the discretized 2D geometry is then extended along the translation-invariant direction (i.e., the z-axis) by superimposing fault elements over their horizontal faces without shearing any stress grid point.

As discussed by Cruz-Atienza (2006), many different fault-element structures may be considered. However, the structure presented in this section (Figure 2) offers the best compromise between stress-field resolution ahead of the rupture front and geometric flexibility to discretize nonplanar faults.

Rupture-boundary conditions

Because our rupture model should handle nonplanar faults in arbitrarily heterogeneous media, we do not solve for the Cauchy-mixed boundary-value problem associated with planar faults in a homogeneous space (e.g., Madariaga, 1976; Das and Aki, 1977; Virieux and Madariaga, 1982). On the contrary, we solve for a simpler boundary-value problem in which only the stress drop associated with the material dislocation is considered as a boundary condition. We assume no opening in the rupture process, so the associated stress drop always takes place in the tangential fault direction describing either fracture modes II or III (i.e., in-plane and antiplane modes, respectively). In our rupture model, every fault element acts as an independent unit, inside which the same boundary condition is applied. This means that, depending on the local fault orientation in a given element, the same shear-stress drop $\Delta \boldsymbol{\tau}$ is imposed on the entire set of stress grid points contained in that element (cubes in Figure 2b).

Following the procedure introduced in the 2D formulation, let us consider a local Cartesian reference frame $x'y'z'$ that matches the fault orientation in a given fault element. As we can see in Figure 3, if one of the local axes points toward the fault-strike direction (e.g., the x'-axis), the local reference frame is determined uniquely by the fault-normal vector. To apply the boundary conditions, we transform the stress tensor $\boldsymbol{\tau}$ from the original Cartesian system xyz to the fault local one by mean of two successive rotations along the Euler angles θ and ϕ:
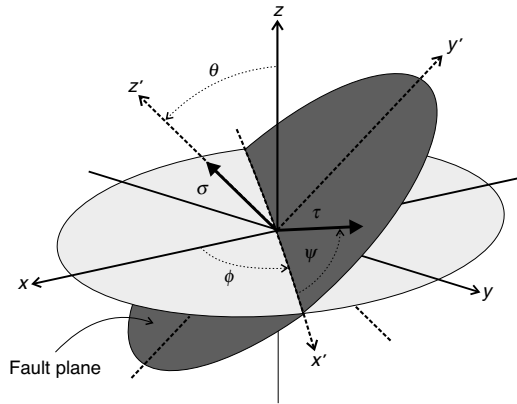

Figure 3. Local reference frame $x'y'z'$ matching the fault orientation in a give source fault element. Quantity σ is the fault-normal stress, and Ψ is the orientation angle of the fault shear stress τ over the fault surface measured from the x' axis.

$$\boldsymbol{\tau}' = \mathbf{A}\boldsymbol{\tau}\widetilde{\mathbf{A}}, \qquad (2)$$

where the 3×3 orthogonal matrix $\mathbf{A}$ is defined by the product of two rotation matrices that depend on the fault dip and fault strike (i.e., angles ϕ and θ in Figure 3). The symbol $\widetilde{\mathbf{A}}$ represents the transposed matrix of $\mathbf{A}$. The normal and shear fault tractions illustrated in Figure 3 are then respectively, given, by two expressions:

$$\sigma = \boldsymbol{\tau}'_{zz} \quad \text{and} \quad \boldsymbol{\tau} = \sqrt{\boldsymbol{\tau}'^{\,2}_{xz} + \boldsymbol{\tau}'^{\,2}_{yz}}. \qquad (3)$$

Once the stress-boundary conditions are applied in the local system, the stress tensor is transformed back into the global one via the following equation,

$$\boldsymbol{\tau} = \widetilde{\mathbf{A}}\boldsymbol{\tau}'\mathbf{A}, \qquad (4)$$

to perform the time integration of system 1a. This procedure shows the general way we apply boundary conditions along an arbitrarily oriented fault element for every time step.

FAULT MECHANICS

Neglecting inelastic damage within the fault zone is usually the first simplification done when modeling rupture dynamics. In other words, one supposes a linearly elastic response of the entire medium except over the infinitely thin, sliding surface in which deformations and stresses are related through a constitutive friction law. In this case, off-fault inelastic processes are supposed to be integrated into the friction law, which involves both fault kinematics and fault tractions when failure happens. As a consequence, the reliability of the rupture model mainly depends on the accurate estimate of these two interdependent fields.

Rupture kinematics

To estimate slip and slip rate in the 3D geometry, we follow the same strategy introduced by Cruz-Atienza and Virieux (2004) in the 2D geometry. In our 3D configuration, the fault surface always presents a translation-invariant direction that is parallel to one Cartesian axis (e.g., the z-axis in Figure 2b). The procedure for evaluating the fault-kinematic parameters should then be performed according to the local fault element's orientation. We always suppose one of the two local reference axes (i.e., x' or y') to be parallel to such an invariant direction.

Let the magnitude of the slip vector s be the tangential displacement discontinuity on the fault surface described by the positive (D^+) and the negative (D^-) fault blocks, as assumed in the following equation:

$$s(t, \Phi) = D^+(t, \Phi) - D^-(t, \Phi), \qquad (5)$$

where the time is denoted by t and the constitutive friction law is denoted by the local set of parameters Φ. As shown in Figure 2a, the discrete fault plane passes through the center of the fault element. Thus, velocity grid points i around the cell (black spheres) belong either to the positive or the negative fault block.

To compute the positive fault block displacement D^+, we average the fault-parallel particle displacements u_i^t by integrating the n particle velocities that lie within a small sector (gray zone) around the fault-normal plane (dotted line). This procedure is expressed in the following formula:

$$D^+(t, \Psi) = \frac{1}{n} \sum_{i=1}^{n} u_i^+(t, \theta, \Psi) \cdot \mathcal{H}_i(\theta, \Psi), \qquad (6)$$

where the weight functions $\mathcal{H}_i$ are introduced in the 2D case (Cruz-Atienza and Virieux, 2004) and numerically recomputed for the 3D geometry. Basically, they are normalized functions that make the fault-block-displacement estimate numerically independent of a faulting mechanism. They are computed once for a given finite-difference stencil and then stored for future rupture simulations with an arbitrary fault geometry and a propagating medium. The only difference with respect to the 2D approach is that, in three dimensions, these functions also depend on Ψ, the direction in which the shear stress acts over the fault plane (Figure 3).

For symmetry reasons with respect to the fault-normal axis z', the weight functions may be defined as the following linear combination:

$$\mathcal{H}_i(\theta, \Psi) = |\cos \Psi| \cdot \mathcal{H}_i(\theta, 0°) + |\sin \Psi| \cdot \mathcal{H}_i(\theta, 90°).$$

In other words, the functions $\mathcal{H}_i(\theta, \Psi)$ are obtained from those computed for two specific angles, $\Psi = 0°$ and $\Psi = 90°$. This procedure makes the fault-block displacement (equation 6) independent of the source-rupture mechanism.

As discussed by Cruz-Atienza and Virieux (2004), considering the velocity grid points as lying within the element sector mentioned above (gray zone, Figure 2a) avoids undesirable effects from inter-element destructive interferences. In the specific element structure, we have selected the angle γ (Figure 2), which defines such a region, is equal to 56°. This value means that at least four but no more than eight velocity grid points lie in that sector per fault block, irrespective of the fault orientation with respect to the translation-invariant axis. For instance, in Figure 2b, we have $n = 4$ (see equation 6). Once the negative fault-block displacement D^- is computed in a similar way, we can estimate the fault-element slip function by inputting these values into equation 5. The slip-rate function in a given fault-element is determined in exactly the same way but without integrating the velocity field in the velocity grid nodes.

When simulating the rupture of the same extended planar fault for different dipping angles (i.e., the angle with respect to the translation-invariant axis — for instance, θ if $\phi = 0$; see Figure 3), a small dependence of the average slip and slip-rate functions on that angle remains. For symmetry reasons of the numerical stencil, it is periodic every 90°. This finite-fault-orientation anisotropy is also found in the 2D case and is corrected by introducing a numerically determined normalized factor that depends on θ and multiplies both slip and slip-rate functions. In the 3D case, this factor is given by $f(\theta) = A\theta^3 + B\theta^2 + C\theta + D$, where $A = 0.00004$, $B = -0.003$, $C = 0.06$, and $D = 1.0$; the factor yields the slip and slip-rate functions no longer dependent on fault orientation. In this definition, the angle θ always should be measured from the nearest Cartesian axis to the fault plane.

Figure 4 shows slip and slip-rate functions computed in one fault element displayed in Figure 2 for different fault orientations. These simulations were performed considering a simple linear time-weakening friction (Andrews, 2004) with a characteristic weakening time equal to 0.4 s. Shear tractions drop down linearly from the initial stress level $\tau_0 = 30$ bar to the dynamic level $\tau_s = 0$ bar in exactly that specific time. Because the translation-invariant direction is parallel to the z-axis in this example, following Figure 3 we consider the angle $\theta = 90°$ in our further simulations.

The left column shows slip and slip-rate functions computed for six different fault-orientation angles, $\phi = 0°, 9°, 18°, 27°, 36°, 45°$ and for a shear-stress drop $\Delta\tau$ perpendicular to the translation-invariant direction ($\Psi = 0°$). The right column shows similar results but for $\Delta\tau$ parallel to the translation-invariant direction ($\Psi = 90°$). Nearly no dependence on the fault orientation ϕ is observed, whereas results are slightly dependent on the stress-drop orientation angle Ψ, with an overestimation of amplitudes smaller than 10% for $\Psi = 90°$.

Failure criterion

Rupture propagation is a thermodynamic system in equilibrium. In other words, it is a system in which the balance between the energy-release rate and fracture energy is conserved. That is what Griffith's (1920) criterion states. However, because no real material may resist infinite stress concentrations, an alternative way to determine if rupture keeps going is by looking at the stress field around the rupture front and comparing it with the current fault strength. In our FDFE approach, we adopt the latter strategy as a failure criterion.

To determine the actual state of stress of a given fault element, we monitor the fault tractions via equations 3 in the central point of the element and within a small neighborhood given by the six stress grid points lying at one spatial step from the central point. The algorithm always takes the maximum stress values in these points as the element state of stress. We consider these neighboring points because in nonplanar discrete faults we never know exactly where the continuous fault geometry passes. The hypothesis behind such an approach is that tractions determined in this way represent their mean value along the entire fault element (Das and Aki, 1977).
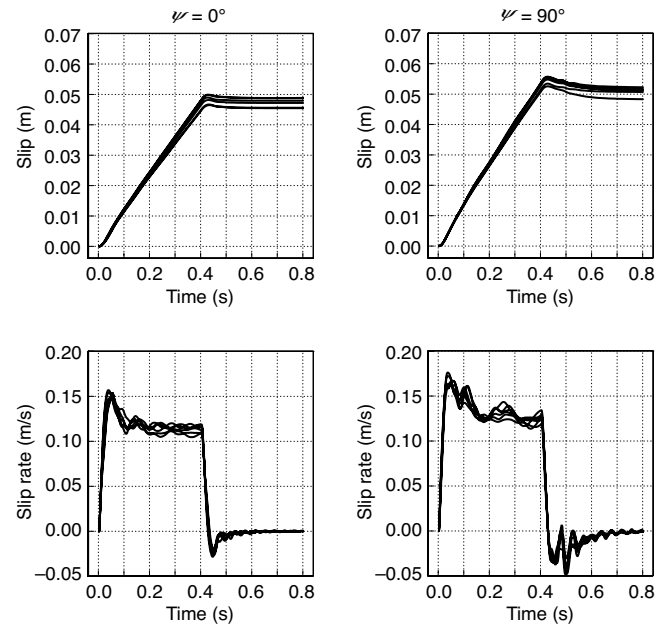

Figure 4. Slip and slip-rate time functions computed in a point source represented by one fault element (Figure 2b). Results were obtained and superimposed in both columns for $\phi = 0°$ and different angles $\theta = 0°, 9°, 18°, 27°, 36°, 45°$ (see Figure 3). The left column corresponds to a shear stress drop $\Delta\tau$ parallel to the x'-axis (i.e., $\Psi = 0°$, Figure 3) and the right column for a $\Delta\tau$ perpendicular to the x'-axis (i.e., $\Psi = 90°$).

Fault strength in our model is governed by a Coulomb-like slip-weakening constitutive law (Ida, 1972; Palmer and Rice, 1973). It can be expressed as

$$\tau_c(\sigma,s) = \tau_s + (\tau_u - \tau_s)\left(1 - \frac{s}{\delta_c}\right)H\left(1 - \frac{s}{\delta_c}\right), \quad (7)$$

where $\tau_u = \sigma\mu_s$ and $\tau_s = \sigma\mu_d$. In these equations, the quantity σ is the fault-normal stress (equation 3), the fault-slip magnitude is denoted by s (equation 5), and the Heaviside step function is $H(\cdot)$. The constitutive parameters of this linear relationship are the static friction coefficient μ_s, the dynamic friction coefficient μ_d, and the slip-weakening critical distance δ_c. Equation 7 may be rewritten as

$$\tau_c(\sigma,s) = \sigma\left[\mu_d + (\mu_s - \mu_d)\left(1 - \frac{s}{\delta_c}\right)H\left(1 - \frac{s}{\delta_c}\right)\right] \quad (8)$$

to see that friction is equal to the normal-fault stress multiplied by a factor that evolves with slip once rupture begins.

The Coulomb friction law states that rupture happens in a given fault point (i.e., fault element) when the ratio between τ and σ (equations 3) at that point equals the current friction coefficient. This condition is equivalent to saying that rupture happens when the fault-shear traction reaches the fault strength, i.e., when $\tau = \tau_c$. Every time this condition occurs, a material dislocation develops because of the progressive drop of fault strength implicit in equation 8. This drop of strength is translated into the stress-boundary conditions described earlier.

RESOLUTION AND CONVERGENCE

In this section, we explore the resolution and convergence of our FDFE model under spontaneous rupture conditions. To achieve this, we analyze the dependence of fault solutions on both the grid size and the slip-weakening critical distance. We first introduce some concepts based on fracture mechanics and then analyze numerical results. However, we do not assess the accuracy of the method in this section because independent reference solutions were not used.

Cohesive-zone analysis

Introduced by Barenblatt (1959), the concept of cohesive force plays a fundamental role in the rupture process because it directly affects the nature of the excited wavefield, especially in the neighborhood of the rupture front where the highest frequencies are concentrated. When dependent on fault slip, these forces remove the stress singularity and make the slip function derivable at the crack tip (Ida, 1972; Palmer and Rice, 1973; Andrews, 1976a). Their evolution as a function of slip then controls the frequency content of the physical solution as well as the width of the so-called cohesive zone Λ_c behind the rupture front. This zone is defined as the fault region inside which the breakdown process takes place — the broken region where the shear stress has not yet reached the dynamic friction level. In the linear slip-weakening model we consider (equation 7), the stress drop in every fault point happens along a critical slip distance δ_c, which then controls both Λ_c and the way stresses concentrate ahead the rupture front.

Our failure criterion assumes that the mean shear stress along a fault element is approximately equal to the stress in the central region of the element. To achieve numerical convergence of the spontaneous rupture problem, element mean stress should not depend on element size, i.e., grid size. In other words, the stress at the center of the element must be representative of the mean value along the whole element (see Das and Aki, 1977). Removing the stress singularity via the slip-weakening mechanism should promote the verification of this condition as the critical distance δ_c increases. This argument holds because the stress gradient ahead of the rupture front in such a nonsingular case becomes much smaller with increments in δ_c. As a consequence, the cohesive zone width Λ_c represents a physical length in which the stress evolution must be well resolved during rupture simulation.

Because δ_c directly controls Λ_c, this constitutive parameter acts as a regularization quantity that should also control numerical convergence through a cohesive-zone resolution parameter that, following Day et al. (2005), may be defined as

$$N_c = \frac{\Lambda_c}{\Omega}. \quad (9)$$

This number represents the number of fault points (fault elements) of length Ω inside the cohesive zone along the direction perpendicular to the rupture front. Because the fault elements have five stress grid points along the diagonals in our numerical simulations (Figure 2), from now on we assume the relation $\Omega = 5h$, where h is the grid size. Thus, we can expect a minimum necessary value of N_c for getting reliable simulation results.

In accordance with this expectation, Day et al. (2005) identify N_c as a suitable convergence parameter for their finite-difference and boundary-integral rupture models and determine a required average value of $N_c \geq 4.4$ for both methods. The finite-difference model introduced by Madariaga et al. (1998) yields stable and reproducible results if $N_c \geq 6.44$; the recently introduced finite-volume approach by Benjemaa et al. (2007) also gives accurate results for $N_c \geq 8$. To understand the properties and limitations of our rupture model, we present a parametric study that explores the influence of the grid size h and the slip-weakening critical distance δ_c on both N_c and some error metrics of fault solutions.

Because the critical distance δ_c is related directly to the rupture energy budget (e.g., Day, 1982; Madariaga and Olsen, 2000), the fairest way to carry out such a parametric study in which this constitutive parameter varies would be to initiate every rupture case from its critical initial patch. In other words, we assume the balance between the available and the absorbed fracture energies at the origin time. If we suppose the relative upper-yield-point parameter $S = (\tau_u - \tau_0)/(\tau_0 - \tau_s)$ to be constant over the fault, then the critical patch radius is directly proportional to the distance δ_c. Given that the other varying parameter is the grid size, computer memory limitations constrain us to consider a relatively small fault, preventing large variations of the nucleation-patch size.

The other possible way to keep the same energy-balance condition for different values of the distance δ_c is by keeping the nucleation-patch size constant and then varying the value of S. Nonetheless, in that case, the governing relation is not linear, making S grow asymptotically as the δ_c decreases. Unrealistically high values of strength excess $(\tau_u - \tau_0)$ relative to the stress drop $(\tau_0 - \tau_s)$ must be then considered when δ_c approaches zero. So, we keep the same nucleation patch size, the same yield stress τ_u, and the same dynamic friction τ_s, whatever the value of δ_c. We only change the initial stress τ_0 such that S ranges linearly from 0.2 for $\delta_c^{\max}$ to 1.0 for $\delta_c^{\min}$. These

limiting values make rupture along the in-plane direction propagate at subshear speeds for all δ_c values when rupture is simulated with the coarsest finite-difference grid.

The problem geometry is shown in Figure 5. Rupture occurs along a vertical right-lateral, strike-slip planar fault embedded into a linearly elastic 3D homogeneous, isotropic medium. The material properties are shown in Table 1. The fault plane is completely surrounded by strength barriers, preventing the rupture from propagating further. Both the initial fault-stress conditions and the constitutive friction parameters are listed in Table 2 (label a). The shear prestress field τ_0 is horizontal and parallel to the fault plane (i.e., parallel to the x reference axis) at all points. Rupture initiation is identical in all rupture simulations.

At time $t = 0$, the shear stress inside the nucleation patch overtakes τ_u, the static yield stress (equation 7), provoking an initial stress drop equal to $\tau_0 - \tau_u$ in that region. In all cases, the relation $\tau_0 = 1.2\tau_u$ is verified inside the nucleation patch at that moment. As mentioned, the initial shear stress outside the nucleation patch is chosen according to the current δ_c value. The slip-weakening-distance tested values are $\delta_c = [0.1 \text{ m}, 0.2 \text{ m}, 0.4 \text{ m}, 0.8 \text{ m}, 1.2 \text{ m}, 1.6 \text{ m}]$. Given the geometry of the fault elements describing the source, it is impossible to discretize both the nucleation patch and the fault plane with the problem being exact dimensions.

We then decide to match exactly the nucleation-patch dimensions by taking the spatial grid steps $h = [24.2 \text{ m}, 46.9 \text{ m}, 88.2 \text{ m}, 157.9 \text{ m}, 214.3 \text{ m}]$. This brings fault-size overestimations ranging from 100 m for $h_{\min}$ to 800 m for $h_{\max}$. In the following, we always take into account this geometric mismatch when estimating uncertainties in the error of fault solutions. All numerical simulations were performed by solving the 3D system 1 using second-order difference operators in time and fourth-order operators in space (see Cruz-Atienza, 2006).

From Ida (1972) results, Andrews (1976a, 2004) derives a theoretical expression for the cohesive-zone length. His analysis shows that if the static-stress drop $\Delta\tau = \tau_0 - \tau_s$ and δ_c are constant over the fault, the width Λ_c of that zone suffers a contraction inversely proportional to L, the rupture-propagation distance. Detailed ener-

gy-balance considerations lead Day et al. (2005) to show that this contraction depends not only on L but also on rupture mode and rupture velocity. Assuming a semi-infinite antiplane crack propagating indefinitely, they deduce a theoretical expression for the cohesive-zone width given by $\Lambda_c = (9/16)(\mu\delta_c/\Delta\tau)^2 L^{-1}$. From this approximation, we compute corresponding values of N_c (equation 9) at the fault point $P1$ (Figure 5) for every δ_c, Ω, and $\Delta\tau$ comprised in our parametric study (Figure 6a).

We do not expect these estimates to correspond with those from our solutions because they assume purely antiplane fracture mode and subshear steady propagation. However, these values may be used as a qualitative reference to understand how a spontaneous rupture behaves when varying both independent parameters h and δ_c. As we shall see, rupture propagation along the in-plane direction (i.e., x-axis direction) in most cases within the parametric domain is subject to the supershear transition. This induces extreme spatial variations of Λ_c, which expands with rupture propagation.

Figure 6 shows, in the middle and bottom panels, average values of the resolution parameter N_c computed with our FDFE rupture model as a function of h and δ_c. These values were computed along two lines passing through the fault center, one parallel to the z-axis (i.e., pure antiplane direction, Figure 6b) and the other parallel to the x-axis (i.e., pure in-plane direction, Figure 6c). To get an approximation of Λ_c along the rupture front, we measure the distance from the center of each fault element at its rupture time to the nearest one in which the shear stress has already reached the dynamic friction level. We then estimate N_c from equation 9.

At first glance, the numerical results appear to be in accordance with general theoretical expectations, i.e., upper panel. Minimum values of N_c correspond to the domain region with smallest δ_c and largest h values, where the cohesive zone is poorly resolved. Conversely, it is well resolved in the domain region with the highest δ_c

Table 1. Material properties of the 3D full space considered in this work. Quantities v_p and v_s are, respectively, the P- and S-wave velocities, and ρ is the density.

v_s (m/s)	v_p (m/s)	ρ (kg/m³)
3464	6000	2670

Table 2. Initial stress conditions and constitutive friction parameters from (a) the Resolution and Convergence section and (b) the Model Validation section. Quantity τ_0 is the initial fault shear stress, σ_0 is the initial fault-normal stress, μ_s is the static friction coefficient, μ_d is the dynamic friction coefficient, and δ_c is the critical slip-weakening distance.

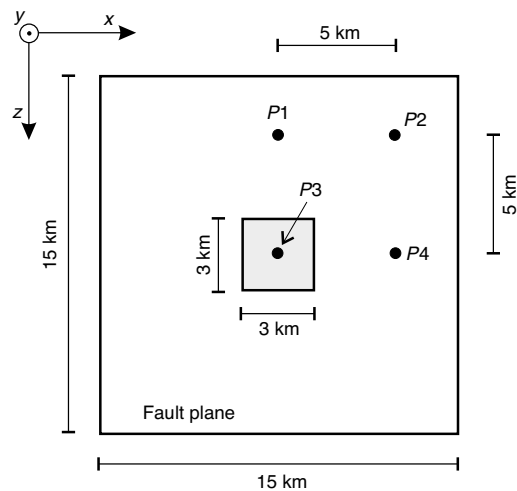| Model parameters	Nucleation	Outside nucleation
τ_0 (a)	81.6 MPa	(varying)
τ_0 (b)	97.49 MPa	73.73 MPa
σ_0 (a,b)	120 MPa	120 MPa
μ_s (a,b)	0.677	0.677
μ_d (a,b)	0.525	0.525
δ_c (b)	0.8 m	0.8 m
δ_c (a)	(varying from 0.2–1.6 m)	

Figure 5. Resolution test problem geometry. The nucleation patch (gray square) is centered in both the along-strike and along-dip fault directions. Fault solutions at the four observation points $P1$, $P2$, $P3$, and $P4$ (black points) are used to estimate the slip and slip-rate function errors.

and smallest h. There, we find values of N_c ranging from about 4 to 17 when considering both fracture modes together. The standard deviations of the mean N_c estimates at the corner of this well-resolved
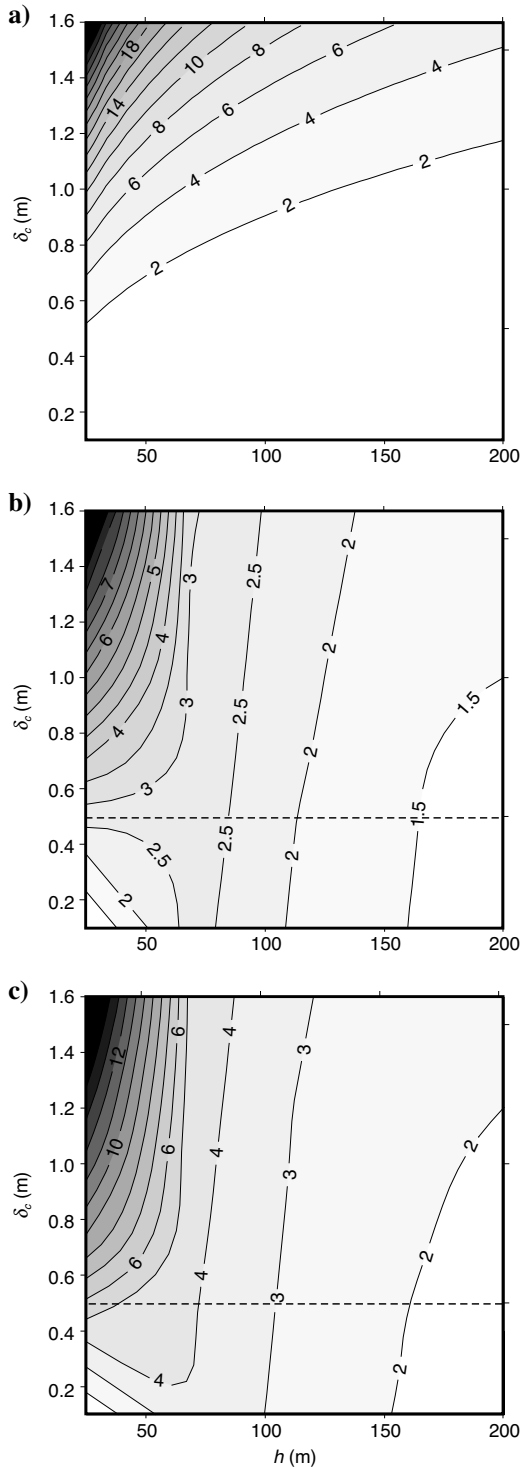

a)

b)

c)

Figure 6. Cohesive-zone-resolution parameter estimates (N_c, equation 9) as a function of the spatial grid increment h and the slip-weakening critical distance δ_c. (a) Theoretical values computed for a semi-infinite subshear antiplane crack. Numerical average values computed with the FDFE approach along the (b) antiplane and (c) in-plane fault directions. Below the dashed lines, N_c estimates are affected substantially by numerical inaccuracies.

domain region are ± 2.7 and ± 6.6, respectively, for the antiplane and in-plane panels. These values reveal a variability of the cohesive zone length Λ_c, with rupture propagation almost 2.5 times larger along the in-plane rupture direction.

Even if they always vary with both parameters, the numerical N_c estimates (middle and bottom panels) over the range $h \in [70 \text{ m}, 200 \text{ m}]$ are less sensitive to the slip-weakening distance δ_c than the theoretical ones (upper panel). However, for $h \lesssim 70$ m and $\delta_c \gtrsim 0.5$ m, both the direction and magnitude of the N_c gradient vectors become similar in the three panels. In this domain region where $N_c \gtrsim 4$, the cohesive-zone sampling rate grows rapidly even when simulating numerically the spontaneous rupture.

A rough estimate of Λ_c from these figures and equation 9 shows that a huge range of cohesive-zone sizes were explored in the parametric analysis (from approximately 121 to 2031 m, with variations of one order of magnitude). Of course, not all of these estimates are correct because numerical inaccuracies may lead to unphysical values. For instance, N_c values associated with the smallest slip-weakening distance for all grid sizes are not well resolved because Λ_c, during the whole rupture, has been smaller than the smallest Ω (121 m), making its estimate impossible. On the other hand, we know that, by definition, N_c cannot increase for a given physical problem with increments in h. For this reason, after inspection of Figure 6, we determined that all estimates of N_c within the domain region below the dashed lines (i.e., for $\delta_c < 0.5$ m) are unreliable because of inaccuracies in rupture simulation and in the procedure determining N_c.

Fault-solutions analysis

We have computed relative errors of fault-solutions with respect to the finest grid case ($h = 24.2$ m) for every δ_c and every h considered in the parametric study. Even if the minimization of these error estimates will not reveal how far numerical solutions are from the physical ones, at least they will improve our understanding of the FDFE numerical convergence and lead us to examine the hypothetical relationship between this convergence and the cohesive-zone resolution parameter N_c. A quantitative comparison with an independent semianalytical solution is then necessary.

Errors were computed for three different fault-solution parameters: rupture times and final slip over the entire fault plane, and the slip-rate time functions in four observational points (Figure 5). The error function is the absolute root mean square (rms) for rupture times and the relative rms for final slip and slip-rate time series. Because of the geometry of the source-fault elements and the stability condition, solutions over the fault plane for different grid increments may not be computed at the same points in space and time. To estimate errors, we then performed both spatial and temporal interpolations of all simulation results, supposing that the information contained over the discrete surfaces corresponds exactly to the fault geometry. This implies a maximum geometric mismatch (near the fault edges) from the spatial interpolation of about 2.5% of the total fault length in the coarsest grid cases ($h = 214.3$ m). Such a mismatch decreases with grid size and has a value of 0.3% in the finest grid ($h = 46.9$ m). Because rupture times are approximately proportional to the rupture propagation distance, we expect the same maximum percentages of uncertainty in the error estimate for the three observed fault parameters.

Time interpolation of the slip and slip-rate functions for different discretizations has been taken as linear; spatial interpolation over the

rupture surface has been carried out in a regular grid with a spatial increment of 100 m. Interpolation values f_{int} of fault-solutions fields $\mathbf{u}_i$ were computed as

$$f_{int} = \sum_{i=1,n} \frac{\mathbf{u}_i}{a_i}, \quad \text{where } a_i = \sum_{j=1,n} \left(\frac{d_i}{d_j}\right)^m. \quad (10)$$

In these equations, quantities a_i are weighting factors that multiply the n punctual fault-solutions lying inside spherical supports of radius r centered at the interpolated values f_{int} and d_i are the distances from f_{int} to each one of these punctual solutions. We always took $m = 0.5$ in this work and $r = 1000$ m in this parametric study. This value of r is the same for all grid sizes and corresponds to the minimum necessary for having at least one fault element inside the spherical interpolation support.

Figure 7 shows error-estimate results for the three selected fault parameters as a function of the grid size h and the slip-weakening critical distance δ_c. The rupture time of one fault point is defined as the time at which the slip rate first exceeds 0.01 m/s at that point. Final slip is measured over the entire fault at the end of each simulation lasting 5 s. Slip-rate function errors correspond to the average rms of the four observational fault points shown in Figure 5. Except for the coarsest simulations ($h \gtrsim 150$ m), almost no error dependence on δ_c is found. The biggest rupture-time and slip-rate errors are found around the bottom-right corner, (i.e., the parameter domain where N_c has the smallest values, Figure 6). The error in the three parameters decreases mainly with the spatial grid step. The convergence rate for rupture times diminishes as $h \rightarrow h_{min}$, evoking the power-law convergence rate observed in the finite-difference split-node and BIE methods (Day et al., 2005). On the contrary, it remains more or less constant for the other two parameters.

Comparing Figure 6b and c with Figure 7, we find good correlation between the cohesive-zone-resolution parameter N_c and the error estimates for grid sizes $h \gtrsim 70$ m: The smaller the value of N_c, the greater the error. However, we find a lack of correlation for finer grids. This lack of correlation may reveal two different things: (1) There exists an upper value of N_c (~ 4) for which there is an over-sampling of the cohesive zone, making N_c have no further influence in numerical convergence, or (2) the influence of N_c on the FDFE model convergence is always negligible with respect to other first-order effects related to mesh refinements (e.g., reduction of numerical oscillations). This ambiguity may be a consequence of a lack in precision of the error estimate as a result of the smoothing associated with the spatial interpolation.

Several comparisons for the critical distance $\delta_c = 0.8$ m between a reference solution (i.e., a solution calculated with the smallest spatial grid step $h = 24.2$ m) and those obtained on coarser grids are presented in Figures 8 and 9. If we focus on the reference solution (solid lines in both figures), we find that rupture-time contours start developing the supershear transition lobes around 0.5 s after rupture initiation in the along-strike direction (in-plane rupture mode). During rupture acceleration, we find a progressive increase in the resolution parameter N_c that, near the fault edges, exceeds several times those values found outside the transitional fault region (e.g., along the antiplane direction). When comparing the slip-rate rms errors on both the in-plane and antiplane directions (Table 3) and looking at the resolution parameter over the entire fault (right column, Figure 8), we find a good correlation between the systematically higher N_c values along the in-plane direction and the smaller misfits of about 10% for all but one grid size in that direction.

Rupture-time degradation with increments of the spatial grid step are in accordance with the progressive drop in cohesive-zone resolution over the entire fault plane (Figure 8). Slip-rate numerical oscillations induce local variations in rupture times that can be observed for $h \lesssim 157.9$ m as small spikes in the rupture-time contours. We also can appreciate how rupture speed in the coarsest grid case remains smaller than the shear-wave velocity because no transitional lobes are exhibited. Rupture time rms errors for these examples are 0.04, 0.11, 0.28, and 0.41s from top to bottom, respectively. The comparison of the slip and slip-rate functions in observational point $P1$
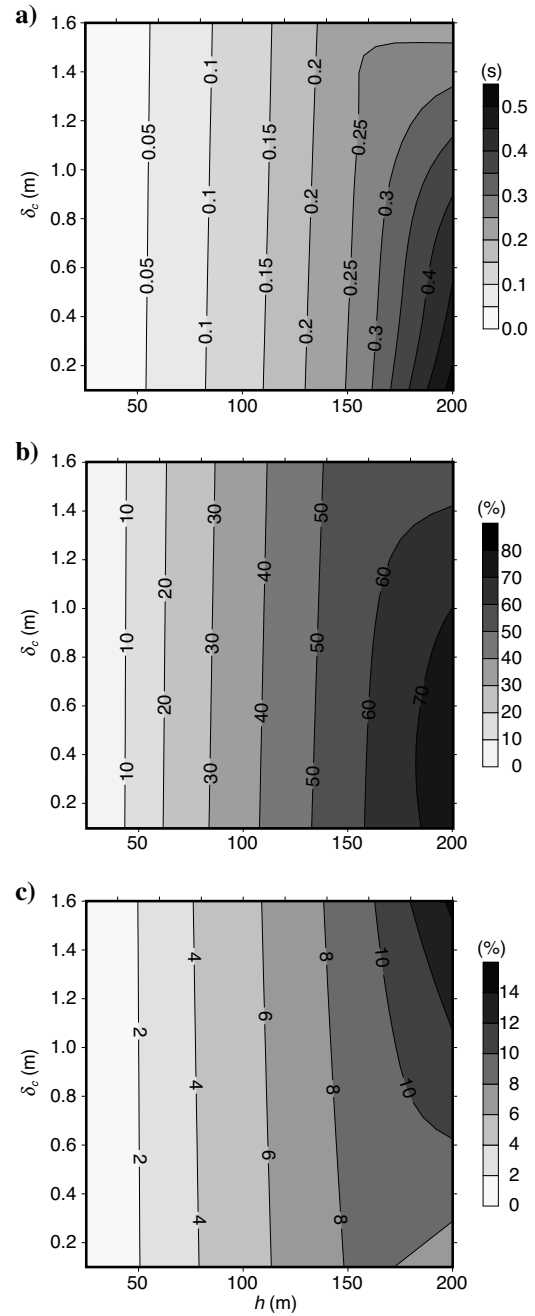

Figure 7. Rupture times (all over the fault) and the slip and slip-rate time function (in four fault points, Figure 5) rms errors computed with respect to the finest grid solutions ($h = 24.2$ m) as a function of the slip-weakening critical distance δ_c and grid size h.

(purely antiplane signals) is shown in Figure 9. Globally, solutions are delayed and noisier with increments in the grid size. Good fits in source parameters and both rupture modes are found for $h \le 88.2$ m (see Table 3 for errors in slip-rate functions). Similar results were obtained in the P4 in-plane mode position but are not shown. The rise time in the antiplane direction is shorter (~ 2.5 s) than in the perpendicular direction (~ 4 s) where the supershear transition takes place. Relative rms errors for final slip over the entire fault range from 2.7% for $h = 46.9$ m to 11.2% for $h = 214.3$ m (see Figure 7). Error in final slip for the coarsest grid represents a mismatch in moment magnitude M_w of about 2%.

MODEL VALIDATION

Consistency between solutions yielded by independent numerical approaches is essential because it is the only way to have confidence in these complex 3D spontaneous-rupture simulations for which no
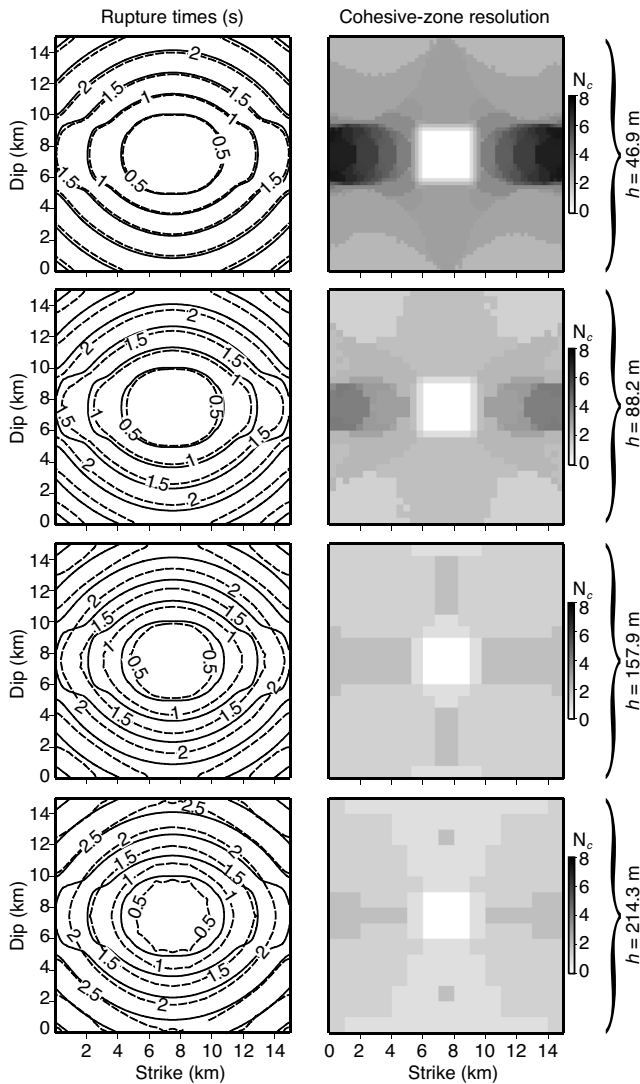
theoretical solutions are available. In the following, we present several numerical exercises that validate our 3D numerical approach for modeling the dynamic rupture along planar and nonplanar faults. We present a quantitative comparison of our FDFE method with a BIE method in terms of rupture times, slip-rate functions, and final-slip rms errors. We use, as a reference, semianalytical solutions computed in the time domain with the BIE method of Aochi et al. (2000b).

Rupture happens along differently shaped strike-slip, left-lateral faults embedded within the same linearly elastic homogeneous and isotropic medium considered in the last section (Table 1). The rupture surfaces follow the equation of a parabola in the x-y plane. The only parameter that varies between the comparison cases is the eccentricity of the conical. The 3D geometry of the faults is then given by a relation of the form

$$f[x, y(x)], \quad \text{where } y(x) = y_0 \pm \sqrt{4a(x - x_0)}. \quad (11)$$

In this equation, x_0 and y_0 correspond to the coordinates of the vertex V of a parabola on the x-y plane with the focus at b (Figure 10). The

Figure 8. Rupture times for the reference case (solid contours) and for coarser grid simulations (dashed contours) at 0.5-s intervals ($\delta_c = 0.8$ m). Right panels show values of N_c for solutions presented with dashed contours in the left panels.
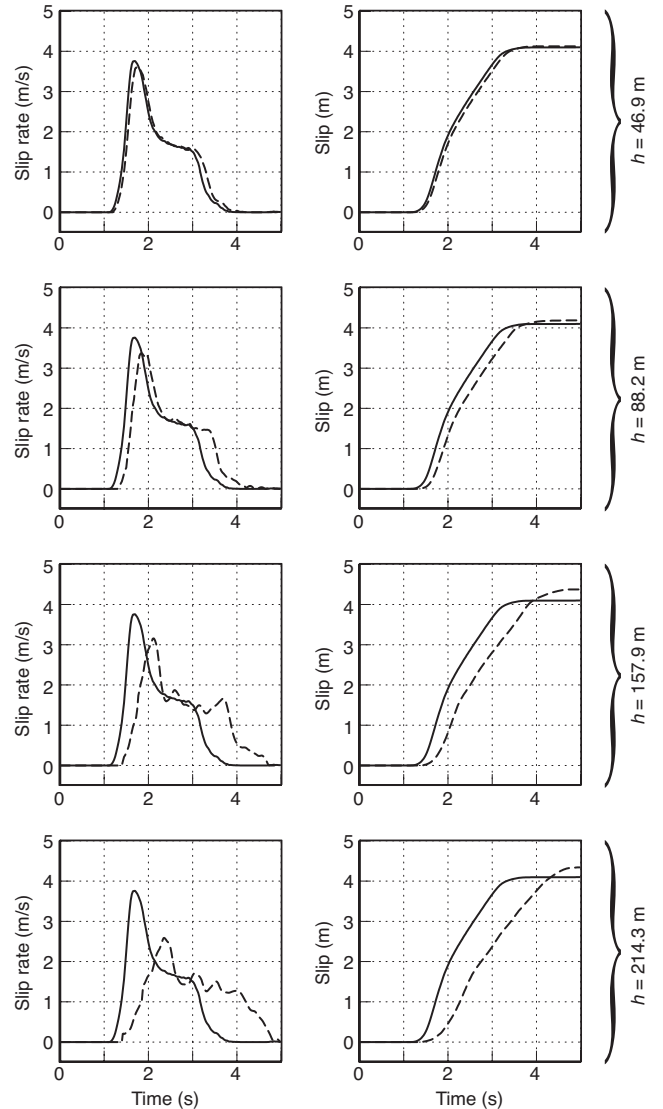
Figure 9. Slip and slip-rate functions computed in the purely antiplane observational point $P1$ (Figure 5) for different spatial grid steps (dashed lines) compared with those of the reference case (solid lines).

coordinate z of all surfaces is translation invariant (Figure 11). The distance between V and b, named a, controls the eccentricity of the conical. As a decreases, the curvature of the rupture surface increases. At the limit as a approaches infinity, the fault becomes planar. In this manner, by changing a, we go from the simple planar case toward a more curved fault. We choose four different geometries. Selected values for a go from ∞ to 18, 10, and 5 km, as shown in Figure 10 for curves $F1$, $F2$, $F3$, and $F4$, respectively. All of these faults are 30 km long in the strike direction and 6 km deep (translation-invariant direction). Figure 11 illustrates a 3D view of the surface, with $a = 10$ km.

The vertex V lies at the center of the surfaces, a location considered as the source origin. The nucleation patch is a square region centered in the source origin with side lengths of 2 km (black patch, Figure 11). For comparisons, we have taken four fault points placed along a horizontal plane passing through V (white cubes). The first observational point, $P1$, coincides with the source origin, and the other three points ($P2$, $P3$, and $P4$) are separated from each other by 4 km as measured over the rupture surface. The external fault boundaries are delimited by a strength barrier forbidding a rupture from propagating beyond them.

The initial normal stress is constant over the entire rupture surface. Only the initial shear stress changes between the nucleation patch and the spontaneous-rupture fault region. We have made these unrealistic assumptions to avoid unnecessary complications that would make the numerical comparison more difficult. Constant tractions along a nonplanar surface may suppose an extremely heterogeneous surrounding stress field. Physical considerations should evolve in future exercises by introducing, for instance, simply shaped barriers and asperities. The only parameter that changes among the four comparison cases is the geometric parameter a, i.e., the fault curvature.

The rupture process follows the same Coulomb-like slip-weakening friction law used earlier. Equation 8 shows that friction resistance is equal to the product of the normal fault stress σ and a factor that evolves linearly with slip once rupture begins. During rupture, normal fault stress is the result of the initial normal stress σ_0 and the dynamic normal stress changes $\Delta\sigma$ (i.e., $\sigma = \sigma_0 + \Delta\sigma$). Thus, similarly to former BIE simulations (Aochi et al., 2000b), we suppose that the slip-weakening friction law does not depend on dynamic changes of normal stresses $\Delta\sigma$. Both the static (τ_u) and the dynamic (τ_s) fault strengths only depend on the initial static tractions during the whole rupture process.

The initial fault-stress constant conditions and the constitutive friction parameters are listed in Table 2b. The shear prestress field τ_0 is everywhere parallel to the x-y plane, producing a potential strike-

slip left-lateral fault dislocation. From values given in Table 2 and equation 8, we get $\tau_u = 81.24$ MPa and $\tau_s = 63$ MPa. These two values along with the initial shear stress τ_0 outside the nucleation patch, give an upper-yield-point parameter $S = 0.7$, which is smaller than 1.63. As pointed out for the first time by Andrews (1976b), one possible consequence of this condition is that rupture propagation undergoes the supershear transition. However, given our choice of the slip-weakening distance and the way rupture nucleates, rupture should propagate a larger distance than the current fault length to reach the energetic condition leading to such supershear bifurcation.

At time $t = 0$, we proceed as for previous examples and make the shear stress in the nucleation patch overtake the yield stress on that zone, producing an instantaneous stress drop $\Delta\tau_0 = \tau_0 - \tau_u$. This initial kick is equal to $0.2\tau_u$ in all cases. Once this initial stress drop happens, rupture propagates spontaneously following the linear slip-weakening Coulomb failure criterion discussed earlier.
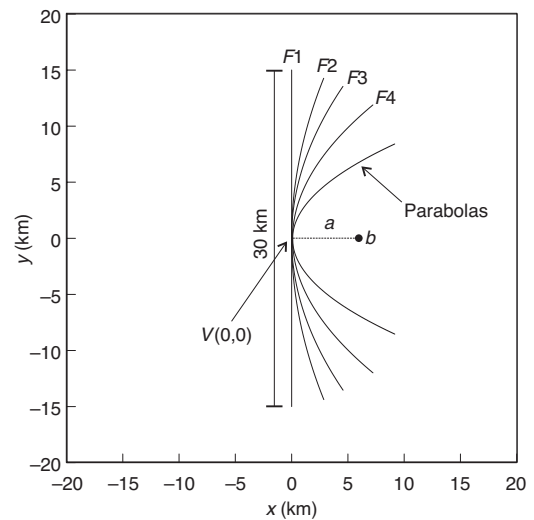

Figure 10. The x-y projection of the 3D nonplanar fault geometries considered in the comparison exercise. These are parabolas given by equation 11. The value $V(x_0, y_0)$ is the vertex of the conicals and b is its focus; a, the distance between these two points, controls the eccentricity. The four selected geometries $F1$, $F2$, $F3$, and $F4$ are all 30 km long and have, respectively, values of ∞, 18, 10, and 5 km for a.
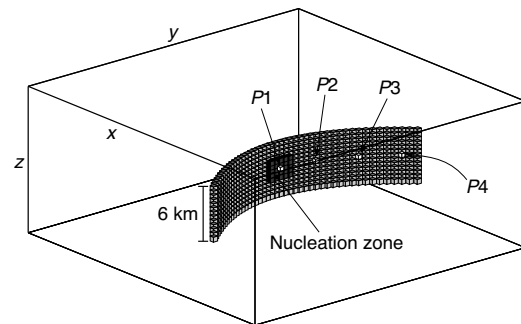

Figure 11. A 3D view of one nonplanar rupture surface used in the comparison exercise. The square nucleation patch (black region) is centered in both the along-strike and along-dip directions and has a side length of 2 km. The four observation fault points (white cubes) are separated by 4 km measured over the fault surface from its center.

Table 3. Relative rms error of slip-rate functions for different grid sizes h with respect to the reference solution (i.e., h = 24.2 m). Values for the antiplane direction correspond to the time series shown in Figure 9.

h (m)	Antiplane (%)	Inplane (%)
46.9	15.9	8.9
88.2	38.7	24.8
157.9	62.9	50.2
214.3	75.1	75.7

The uniform BIE grid interval was fixed to $\Delta s = 0.15$ km, so fault surfaces were discretized by 200×40 square elements in such a way that those element boundaries parallel to the translation-invariant fault axis are contained within the analytic 3D parabolic function. In other words, the centers of the squares shift slightly from the continuous-fault geometry. The corresponding time step was $\Delta t = 0.0125$ s. Nonplanar fault discretization with our FDFE model is not as simple as that because rupture surfaces are represented numerically by parallelepiped fault elements in a regular volumetric grid. Consequently, the distance between the center of these elements depends on the orientation of the fault within the grid.
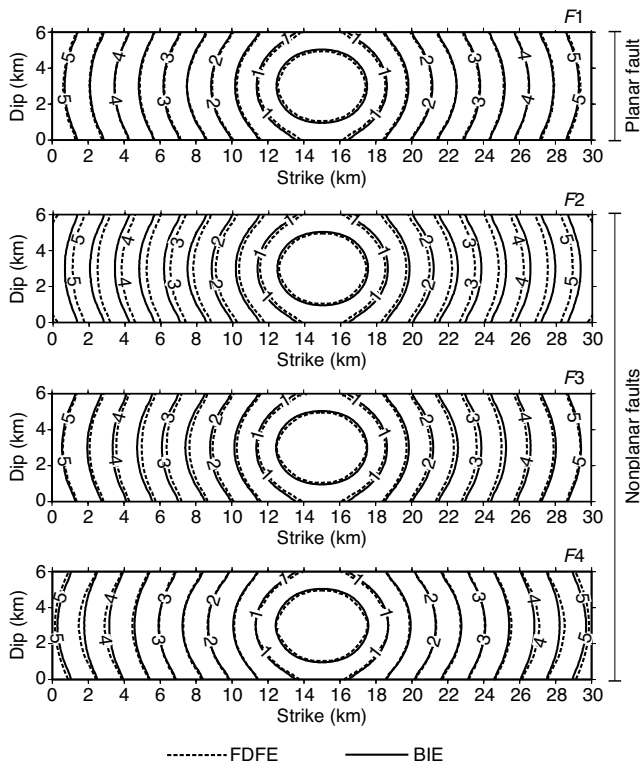

Figure 12. Rupture front contours at 0.5-s intervals computed with the FDFE method (dashed lines) and with the BIE method (solid lines). Comparisons are along a planar fault ($F1$) and along three parabolic surfaces $F2$, $F3$, and $F4$ (see Figure 10).

Table 4. Absolute (rupture times) and relative (slip rate and final fault slip) rms errors of our FDFE method with respect to the BIE reference solutions ($dx = 250$ m). Finite-difference results were obtained with second order in time and fourth order in space accuracy operators (2,4) in a discrete lattice with spatial and time steps of $h = 45.45$ m and $\Delta t = 0.005$ s, respectively.

Fault geometry	Rupture times (s)	Slip rate (%)	Final slip (%)
Planar ($F1$)	0.03	32.7	23.1
Nonplanar ($F2$)	0.10	33.3	15.7
Nonplanar ($F3$)	0.05	30.4	19.9
Nonplanar ($F4$)	0.04	27.1	25.7

As described earlier, source-fault elements are placed alongside each other as closely as possible to the analytic source geometry (Figure 11), so the number of fault element in the along-strike direction changes with fault curvature (i.e., with values of a). To discretize the nucleation patch with the exactly stated dimensions, we took the spatial grid interval $h = 45.45$ m and a corresponding time step $\Delta t = 0.005$ s. Thus, the number of fault elements along the fault strike ranges from 133 in the planar case (surface $F1$, Figure 10) to 175 in the most curved fault (surface $F4$). On the contrary, it remains constant in the along-dip direction (translation-invariant axis) independently of the quantity a and equal to 27. A simple calculation shows us that the current fault dimensions in the planar case are slightly different from those stated in our problem geometry (6 $\times$ 30 km). The greatest discrepancy, 1.5% of the corresponding fault length, is found in the along-dip direction. Similar percentages are found in the nonplanar geometries even in the along-strike direction.

As discussed previously, the geometry of the source-fault elements prevents the exact discretization of both the nucleation patch and entire fault sizes. To make the comparison of fault solutions possible, we performed a spatial interpolation of results yielded by both methods, supposing that all information contained along the discrete surfaces corresponds exactly to the fault-problem geometry. Consequently, estimations of rupture times and location of the observation points have an uncertainty of the same order, of about 1.5%. The regular spatial-interpolation increment is 100 m with a spherical support $r = 600$ m (see equation 10).

The rupture-time contours computed with FDFE (dashed lines) for the planar and nonplanar surfaces are shown in Figure 12 and are compared with those yielded by the BIE approach (solid lines). Very good agreement is observed in all rupture surfaces. In the planar case (surface $F1$), except for quite small differences at the very beginning of the process, FDFE rupture propagation is almost identical to the reference solutions. In the nonplanar cases (surfaces $F2$, $F3$, and $F4$), even if rupture times are very close to the reference ones, it turns out that FDFE rupture propagates faster with increments on the fault curvature (i.e., as the orientation of the fault surface approaches 45° with respect to the Cartesian reference frame). Despite this anisotropic effect, the absolute rms error for all cases remains smaller than or equal to 0.1 s (Table 4).

Figure 13 shows the slip-rate time series computed in four observation fault points (see Figure 11) with both the FDFE (dashed lines) and BIE (solid lines) methods. Signals are not filtered. Low frequency spurious oscillations appear as a result of the stress-drop rates associated with the slip-weakening critical distance $\delta_c = 0.8$ m. An overestimation of the slip-rate functions with respect to the BIE approach is observed systematically and translated into relative rms errors of about 30% in all rupture cases (Table 4). The corresponding relative rms errors of the final slip along the entire fault surface range between 15% and 25% (Table 4), which is negligible when considering the uncertainies on seismic moment determination via the widely used kinetic source inversions. BIE solutions with a coarser discretization ($\Delta s = 0.25$ km) were also computed, and no relevant differences from those presented here were found (Cruz-Atienza, 2006). The discrepancy of slip-rate rms errors between the FDFE and BIE methods for both BIE fault discretizations are smaller than 7% of total rms values, proving that the semianalytical reference solutions used in this section basically have converged to the physical ones.

As a whole, the reference BIE solutions are reproduced well by the FDFE approach. These results validate our rupture-boundary

conditions as well as the adopted failure criterion. The slip-weakening spontaneous rupture problem along nonplanar (curvilinear) fault surfaces has been solved successfully by a thick-fault, finite-difference method in a regular Cartesian grid.

DISCUSSION

The FDFE rupture model is implemented in a partially staggered grid where both the velocity vector and the stress tensor are defined by two independent grids shifted halfway between the spatial grid step in the three Cartesian directions. It basically represents an extension of the 2D rupture model proposed by Cruz-Atienza and Virieux (2004). The source is described numerically by a fault zone with a finite width. The fault zone is composed of independent fault elements in which a local set of boundary conditions is applied, depending on the local fault orientation. For an accurate slip and slip-rate estimate, weight functions have been constructed once and then stored for future simulations. The use of these functions makes the evaluation of the source kinematic parameters independent of fault orientation with respect to the numerical grid reference frame.

The two-dimensional analysis performed by Cruz-Atienza and Virieux (2004) has shown that numerical oscillations are controlled by a scaling law relating the number of stress points per fault element to the grid size. The greater the number of points, the smaller the spatial grid step. However, when modeling huge 3D rupture scenarios, computational power limitations prevent the use of extremely fine meshes, so low-order fault elements (i.e., elements with few stress grid points) should be preferred while achieving good accuracy for rupture and wave propagation. The specific element structure we have selected offers good compromise between its size in a feasible 3D mesh and the spontaneous-rupture resolution. If a nonregular grid were implemented in the source region or if the message passing interface (MPI) were used to parallelize the current sequential code, a finer model sampling would be possible; so higher-order fault elements could be used to reduce numerical oscillations and then improve the accuracy, as we have observed in 2D geometries.

Imposing dynamic-rupture boundary conditions always makes the stability condition of numerical methods more restrictive. However, values for the Courant number up to $v_{max}\Delta t/h = 0.66$ yield stable solutions with both second- and fourth-order spatial operators when simulating the spontaneous rupture in the partly staggered grid (see Cruz-Atienza, 2006).

We have implemented a Coulomb-like slip-weakening friction law. Both cohesive-zone resolution and fault-solutions error have been investigated through a parametric study. Numerical N_c estimates for $h \lesssim 70$ m and $\delta_c \gtrsim 0.5$ m are in reasonable agreement with theoretical values for a similar but simpler problem. In this parametric domain region, we always found $N_c \gtrsim 4$. We have also found a good correlation between N_c and error estimates for grid sizes $h \gtrsim 70$ m: the smaller the parameter N_c, the greater the error. However, we find no more correlation for finer grids. This lack of correlation may reveal either an oversampling of the cohesive zone from $N_c \gtrsim 4$, which makes this parameter have no further influence on numerical convergence, or that convergence of the FDFE model is governed mainly by other first-order effects associated with mesh refinement, such as the reduction of numerical oscillations. Fault-error estimates have been computed from interpolated solutions, so the ambiguity associated with the lack of error sensitivity on δ_c may be partly a consequence of inaccurate error estimates.

Comparisons of results obtained by the FDFE rupture model with those obtained by the BIE approach were carried out for planar and nonplanar fault geometries. These comparisons are not trivial. The FDFE method presents a linear convergence rate (Figure 7), that is lower than the power-law rates determined by Day et al. (2005) for two independent and accurate approaches along planar faults: a finite-difference split-node (DFM) model and a frequency domain BIE model. Comparisons presented in this paper as well as the analysis of a well-established benchmark exercise (Harris and Archuleta, 2004) performed by Cruz-Atienza (2006) with the FDFE approach show that values of grid size $h \lesssim 70$ m provide reliable results for different spontaneous-rupture problems, including nonplanar fault geometries. The accuracy of FDFE modeling, which is formulated in the partially staggered grid, is comparable to that of the stress-glut method, which may be implemented in the standard staggered grid for simulating simple planar problems (Dalguer and Day, 2006). Our results show that thick-fault discrete models may provide accurate results even along nonplanar rupture surfaces, provided that suitable treatment of boundary conditions is performed.

Even if dynamic-rupture effects on fault-normal stresses were not taken into account in validating our model, the FDFE method under complex geometric conditions reproduces solutions obtained by an independent semianalytical BIE method quite well (Aochi et al.,
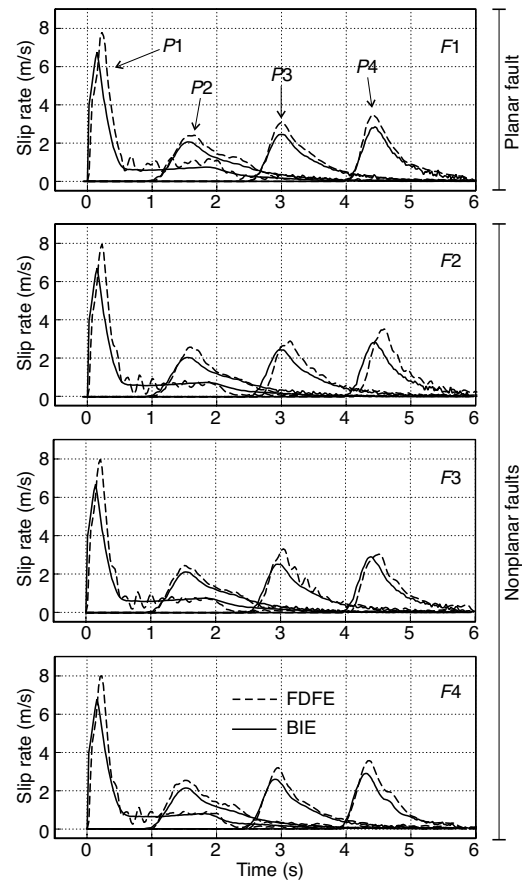

Figure 13. Slip-rate functions computed in four observation fault points (see Figure 11) with the FDFE approach (dashed lines) and with the BIE method (solid lines). Comparisons are along a planar fault ($F1$) and along three parabolic surfaces $F2$, $F3$, and $F4$ (see Figure 10). Signals are not filtered.

2000b). We notice Aochi et al. (2002) show that rupture propagation along nonplanar faults is mainly governed by the shear-stress field ahead of the rupture front even when the Coulomb failure criterion is considered. Dynamic variations of fault strength associated with normal stress changes away from the free surface only cause second-order effects.

CONCLUSION

We have introduced a numerical method based on finite differences in a partially staggered grid for modeling the dynamic rupture of nonplanar faults in three dimensions. This FDFE approach has a specific way of handling boundaries in which a local set of rupture conditions is applied, depending on both the local fault orientation and the constitutive friction law.

The most important feature of the FDFE model is not its accuracy at a given discretization level but the ability to go beyond simple and often unrealistic planar fault geometries. This model has been designed for solving the dynamic rupture problem of nonplanar faults in arbitrarily heterogeneous media. For this reason, validating it in conditions more complex than planar is fundamental. Results obtained for spontaneous slip-weakening ruptures along parabolic faults with a translation-invariant axis are in good agreement with results obtained by a semianalytical BIE method.

The analysis of more realistic nonplanar fault simulations, considering heterogeneous stress fields and variations on the medium properties, are the next modeling target for the 3D FDFE approach, which benefits partially staggered finite-different efficiency. This numerical tool may be applied for studying the dynamic development of complex microfracture networks in oil reservoirs subjected to some regional load by analyzing the associated seismic emissions recorded in both the earth's surface and boreholes. It may be also used to analze nonplanar fault interaction and for the dynamic modeling of large-scale seismic events.

APPENDIX A

A PARTIALLY STAGGERED SECOND-ORDER OPERATOR

If second-order centered finite differences are used to approximate first-order spatial differentiations of a discrete field $\Phi_{i,j,k}$ along the three Cartesian directions x, y, and z within the partially staggered lattice shown in Figure 1 (Saenger et al., 2000), we get, respectively, the following formula:

$$\frac{\partial \Phi_{i,j,k}}{\partial x} \approx \frac{1}{4h}\big(\Phi_{i+1/2,j+1/2,k+1/2} - \Phi_{i-1/2,j-1/2,k-1/2}$$
$$+\ \Phi_{i+1/2,j+1/2,k-1/2} - \Phi_{i-1/2,j-1/2,k+1/2}$$
$$+\ \Phi_{i+1/2,j-1/2,k+1/2} - \Phi_{i-1/2,j+1/2,k-1/2}$$
$$+\ \Phi_{i+1/2,j-1/2,k-1/2} - \Phi_{i-1/2,j+1/2,k+1/2}\big),$$

$$(12a)$$

$$\frac{\partial \Phi_{i,j,k}}{\partial y} \approx \frac{1}{4h}\big(\Phi_{i+1/2,j+1/2,k+1/2} - \Phi_{i-1/2,j-1/2,k-1/2}$$
$$+\ \Phi_{i+1/2,j+1/2,k-1/2} - \Phi_{i-1/2,j-1/2,k+1/2}$$
$$-\ \Phi_{i+1/2,j-1/2,k+1/2} + \Phi_{i-1/2,j+1/2,k-1/2}$$
$$-\ \Phi_{i+1/2,j-1/2,k-1/2} + \Phi_{i-1/2,j+1/2,k+1/2}\big),$$

$$(12b)$$

$$\frac{\partial \Phi_{i,j,k}}{\partial z} \approx \frac{1}{4h}\big(\Phi_{i+1/2,j+1/2,k+1/2} - \Phi_{i-1/2,j-1/2,k-1/2}$$
$$-\ \Phi_{i+1/2,j+1/2,k-1/2} + \Phi_{i-1/2,j-1/2,k+1/2}$$
$$+\ \Phi_{i+1/2,j-1/2,k+1/2} - \Phi_{i-1/2,j+1/2,k-1/2}$$
$$-\ \Phi_{i+1/2,j-1/2,k-1/2} + \Phi_{i-1/2,j+1/2,k+1/2}\big),$$

$$(12c)$$

where h is the grid size of the regular mesh. The discrete expressions for the entire system 1 with second order in time and fourth order in space accuracies are reported by Cruz-Atienza (2006).

REFERENCES

Aagaard, B., 2000, Finite-element simulation of earthquakes: Ph.D. thesis, California Institute of Technology.

Adda-Bedia, M., and R., Madariaga, 2005, Dynamic rupture of a fault kink in antiplane model: EOS Transactions of the American Geophysical Union, **86**, S52A-01.

Ampuero, J. P., J. P. Vilotte, and F.-J. Sánchez-Sesma, 2002, Nucleation of rupture under slip dependent friction law: Simple models of fault zone: Journal of Geophysical Research, **107**, http://dx.doi.org/10.1029/2001JB000452.

Ando, R., T. Tada, and T. Yamashita, 2004, Dynamic evolution of a fault system through interactions between fault segments: Journal of Geophysical Research, **109**, B05303, http://dx.doi.org/10.1029/2003JB002665.

Andrews, D. J., 1976a, Rupture propagation with finite stress in antiplane strain: Journal of Geophysical Research, **81**, 3575–3582.

——, 1976b, Rupture velocity of plane strain shear cracks: Journal of Geophysical Research, **81**, 5679–5687.

——, 2004, Rupture models with dynamically determined breakdown displacement: Bulletin of the Seismological Society of America, **94**, 769–775.

Aochi, H., and E. Fukuyama, 2002, Three-dimensional nonplanar simulation of the 1992 Landers earthquake: Journal of Geophysical Research, **107**, http://dx.doi.org/10.1029/2000JB000061.

Aochi, H., E. Fukuyama, and M. Matsu'ura, 2000a, Selectivity of spontaneous rupture propagation on a branched fault: Geophysical Research Letters, **27**, 3635–3638.

——, 2000b, Spontaneous rupture propagation of on a non-planar fault in 3D elastic medium: PAGEOPH, **157**, 2003–2027.

Aochi, H., R. Madariaga, and E. Fukuyama, 2002, Effect of normal stress during rupture propagation along nonplanar faults: Journal of Geophysical Research, **107**, http://dx.doi.org/10.1029/2001JB000500.

Aochi, H., O. Scotti, and C. Berge-Thierry, 2005, Dynamic transfer of rupture across differently oriented segments in a complex 3-D fault system: Geophysical Research Letters, **32**, http://dx.doi.org/10.1029/2005GL024158.

Barenblatt, G. I., 1959, Concerning equilibrium cracks forming during brittle

fracture: The stability of isolated cracks, relationships with energetic theories: Journal of Applied Mathematics and Mechanics, **23**, 1273–1282.

Benjemaa, M., N. Glinsky-Olivier, V. M. Cruz-Atienza, J. Virieux, and S. Piperno, 2007, Dynamic non-planar crack rupture by a finite volume method: Geophysical Journal International, http://dx.doi.org/10.1111/j.1365–246X.2006.03500.x.

Berenger, J. P., 1994, A perfectly matched layer for the absorption of electromagnetic waves: Journal of Computational Physics, **114**, 185–200.

Collino, F., and C. Tsogka, 2001, Application of the perfectly matched absorbing layer model to the linear elastodynamic problem in anisotropic heterogeneous media: Geophysics, **66**, 294–307.

Cruz-Atienza, V. M., 2006, Rupture dynamique des faille non-planaires en différences finies: Ph.D. thesis, University of Nice Sophia.

Cruz-Atienza, V. M., and J. Virieux, 2004, Dynamic rupture simulation of non-planar faults with a finite-difference approach: Geophysical Journal International, **158**, 939–954.

Cruz-Atienza, V. M., J. Virieux, H. Aochi, and S. Peyrat, 2004, 3D non-planar finite difference dynamic rupture: Application to the Landers earthquake: Geophysical Journal International, **158**, 939–954.

Cruz-Atienza, V. M., J. Virieux, and S. Operto, 2002, Dynamic rupture simulation of bending faults with a finite difference approach: EOS Transactions of the American Geophysical Union, **83**, NG21B-0941.

Dalguer, L. A., and S. M. Day, 2006, Comparison of fault representation methods in finite difference simulations of dynamic rupture: Bulletin of the Seismological Society of America, **96**, 1764–1778.

Das, S., and K. Aki, 1977, A numerical study of two-dimensional spontaneous rupture propagation: Geophysical Journal of the Royal Astronomical Society, **50**, 643–668.

Day, S. M., 1982, Three-dimensional simulation of spontaneous rupture: The effect of nonuniform prestress: Bulletin of the Seismological Society of America, **72**, 1881–1902.

Day, S. M., L. A. Dalguer, N. Lapusta, and Y. Liu, 2005, Comparison of finite difference and boundary integral solutions to three-dimensional spontaneous rupture: Journal of Geophysical Research, **110**, B12307, http://dx.doi.org/10.1029/2005JB003813.

Ely, G., B. Minster, and S. Day, 2006, Large scale dynamic rupture modeling with realistic geometry: EOS Transactions of the American Geophysical Union, **87**, S41C-1350.

Griffith, A. A., 1920, The phenomena of rupture and flow in solids: Philosophical Transactions of the Royal Society of London, **A221**, 163–198.

Harris, R. A., and R. J. Archuleta, 2004, Earthquake rupture dynamics: Comparing the numerical simulation methods: EOS, **85**, 321.

Ida, Y., 1972, Cohesive force across the tip of a longitudinal-shear crack and griffith's specific surface energy: Journal of Geophysical Research, **77**, 3796–3805.

Kame, N., J. Rice, and R. Dmowska, 2003, Effect of prestress state and rupture velocity on dynamic fault branching: Journal of Geophysical Research, **108**, http://dx.doi.org/10.1029/2002JB002189.

Madariaga, R., 1976, Dynamics of an expanding circular fault: Bulletin of the Seismological Society of America, **66**, 639–666.

Madariaga, R., and J. Ampuero, 2005, Rupture dynamics of a geometrically complex fault: EOS Transactions of the American Geophysical Union, **86**, S34A-01.

Madariaga, R., and K. B. Olsen, 2000, Criticality of rupture dynamics in 3-D: Pure and Applied Geophysics, **157**, 1981–2001.

Madariaga, R., K. B. Olsen, and R. J. Archuleta, 1998, Modeling dynamic rupture in a 3D earthquake fault model: Bulletin of the Seismological Society of America, **88**, 1182–1197.

Marcinkovich, C., and K. Olsen, 2003, On the implementation of perfectly matched layers in a three-dimensional fourth-order velocity-stress finite difference scheme: Journal of Geophysical Research, **108**, http://dx.doi.org/10.1029/2002GB002235.

Mikumo, T., and T. Miyatake, 1978, Dynamical rupture process on a three-dimensional fault with non-uniform frictions and near field seismic waves: Geophysical Journal of the Royal Astronomical Society, **54**, 417–438.

——, 1993, Dynamic rupture processes on a dipping fault, and estimate of stress drop and strength excess from the results of waveform inversion: Geophysical Journal International, **112**, 481–496.

Oglesby, D., 1999, Earthquake dynamics on dip-slip faults: Ph.D. thesis, University of California.

Oglesby, D. D., S. M. Day, and D. R. H. O'Connell, 2003, Dynamic and static interaction of two thrust faults: A case study with general implications: Journal of Geophysical Research, **108**, http://dx.doi.org/10.1029/2002JB002228.

Olsen, K. B., R. Madariaga, and R. J. Archuleta, 1997, Three-dimensional dynamic simulation of the 1992 Landers earthquake: Science, **278**, 834–838.

Palmer, A., and J. R. Rice, 1973, The grow of slip surfaces in the progressive failure of overconsolidated clay: Proceedings of the Royal Society of London, series A, **332**, 527–548.

Royer, J.-J., and J.-C. Voillemont, 2005, Estimating heterogeneous reservoir permeability from induced microseismicity: 75th Annual International Meeting, SEG, Expanded Abstracts, 1393–1396.

Saenger, E. H., N. Gold, and S. A. Shapiro, 2000, Modeling the propagation of elastic waves using a modified finite-difference grid: Wave Motion, **31**, 77–92.

Shapiro, S. A., S. Rentsch, and E. Rothert, 2005, Characterization of hydraulic properties of rocks using probability of fluid-induced microearthquakes: Geophysics, **70**, no. 2, F27–F34.

Shapiro, S. A., E. Rothert, V. Rathz, and J. Rindschwentner, 2002, Characterization of fluid transport properties of reservoirs using induced microseismicity: Geophysics, **67**, 212–220.

Vilotte, J., G. Festa, and R. Madariaga, 2005, Spectral element simulations of rupture dynamics along kinked faults: EOS Transactions of the American Geophysical Union, **86**, S34A-02.

Virieux, J., 1986, P-SV wave propagation in heterogeneous media, velocity-stress finite difference method: Geophysics, **51**, 889–901.

Virieux, J., and R. Madariaga, 1982, Dynamic faulting studied by a finite difference method: Bulletin of the Seismological Society of America, **72**, 345–369.

Zhang, W., T. Iwata, and K. Irikura, 2006, Dynamic simulation of a dipping fault using a three-dimensional finite difference method with nonuniform grid spacing: Journal of Geophysical Research, **111**, B05301, http://dx.doi.org/10.1029/2005JB003725.